Slope failure with the material point method

An investigation of post-peak material behaviour

Vardon, Phil; Wang, Bin; Hicks, Michael

Citation (APA)
Vardon, P., Wang, B., & Hicks, M. (2017). Slope failure with the material point method: An investigation of post-peak material behaviour. In *Proceedings of the 15th International Conference of the International Association for Computer Methods and Advances in Geomechanics : 19-23 October 2017, Wuhan, China*

Important note
To cite this publication, please use the final published version (if applicable).
Please check the document version above.

Slope failure with the material point method: an investigation of post-peak material behaviour

P.J. Vardon[a,b]*, B. Wang[a,b] and M.A. Hicks[a]

*a*Geo-Engineeing Section, Delft University of Technology, the Netherlands
*b*State Key Laboratory of Geomechanics and Geotechnical Engineering, Institute of Rock and Soil Mechanics, Chinese Academy of Sciences, Wuhan 430071, China
* P.J.Vardon@tudelft.nl

Abstract

The material point method (MPM) has the potential to simulate the onset, the full evolution and the final condition of a slope failure. It is a variant of the finite element method (FEM), where the material is able to move through the mesh, thereby solving one of the major problems in FEM of mesh tangling. The post-peak material behaviour is shown here to be of importance to characterise the failure, with an exploratory sensitivity analysis being presented highlighting the differences in the simulations. Realistic failure modes can be observed.

Keywords: material point method, slope failure, strain-softening

1. Introduction

Typical slope stability analyses, using, for example, the finite element method (FEM) or the limit equilibrium method (LEM), focus on the initiation of slope failure. However, in general an initial failure tells us little about the risk of failure. For example, a very large failure volume which only causes minor deformations (e.g. 10s of cm or less) may not cause significant damage or threat to life, whereas an initially small slope failure volume, or a superficial slide, may trigger a series of slides due to changes in geometry or stress level, and pose a much greater risk. Standard FEM is often unable to simulate the full failure behavior due to mesh tangling during large deformations, causing the Jacobian matrix to become indeterminant and the calculation to fail. The material point method (MPM) [1], which is based on FEM, addresses this issue by allowing points of material to move through a background mesh which is periodically reset and therefore does not tangle.

By extending simulations from only failure initiation to full failure evolution, the modelled material behavior also needs to reflect post-failure behaviour. This paper explores the use of a simple material model, which explicitly includes post-failure (or post-peak) material behaviour, to investigate how slope failure evolution is influenced by this behaviour. It is based on a series of papers where the formulation has been presented [2] and slope failures have been investigated [3] including the influence of spatial heterogeneity [4] and unsaturated hydro-mechanical behavior [5]. It has also formed the basis of a PhD thesis [6].

2. Theoretical formulation

2.1 Methodology

The governing equations within the model are the same as for slope stability calculations using FEM, or more generally the conservation of momentum. Dynamic effects, which are often eliminated in FEM to give a set of governing equilibrium equations, are included, as momentum is not insignificant during the post-failure motion. Both total stress (single phase) and effective stress (two phase) formulations have been implemented. The formulation given herein is for the two phase formulation, which gives the single phase formulation by considering the degree of saturation to be zero, although the solution algorithm is different [2,5].

The conservation of momentum for the water and the mixture are, respectively,

$$\rho_w \mathbf{a}_w = \nabla p_w + \rho_w \mathbf{b} - \frac{nS_w \mu_w}{k} \cdot (\mathbf{v}_w - \mathbf{v}_s) \tag{1}$$

$$(1-n)\rho_s \mathbf{a}_s + nS_w \rho_w \mathbf{a}_w = \nabla \cdot \boldsymbol{\sigma} + (1-n)\rho_s \mathbf{b} + nS_w \rho_w \mathbf{b} \tag{2}$$

where ρ is the density, $\mathbf{a}$ is the acceleration, p_w is the pore water pressure, n is the porosity, S_w is the degree of water saturation, μ_w is the water viscosity, k is the soil permeability, $\mathbf{v}$ is the velocity, t is time, $\boldsymbol{\sigma}$ is the Cauchy stress, $\mathbf{b}$ is the body force due to, for example, gravity, and subscripts s and w indicate the solid and liquid phases, respectively.

Bishop's stress is used for the stress on the soil skeleton, with the effective stress parameter selected to be the degree of saturation. Hence,

$$\boldsymbol{\sigma}' = \boldsymbol{\sigma} - \mathbf{m}(S_w p_w) \tag{3}$$

where $\mathbf{m}$ is a vector allowing the pore pressure to act only isotropically and is $[1\ 1\ 1\ 0]^T$ for 2D analyses.

The conservation of solid mass is automatic as the solid mass of particles does not change. The mass conservation of the water is utilised to calculate the pore water pressure and, via Darcy's law, the velocity of water. The pore water pressure is given as

$$\frac{dp_w}{dt} = \left(n\lambda - n\frac{S_w}{K_w} \right)^{-1} \left(nS_w \nabla \mathbf{v}_w + (1-n)S_w \nabla \mathbf{v}_s \right) \tag{4}$$

where λ is the rate of change of saturation with change in suction and K_w is the bulk modulus of water.

The discretisation of Eqs. (1) and (2) is undertaken via typical finite element procedures, with the exception of utilising material point locations and properties to perform numerical integration.

2.2 Solution algorithm

Either explicit or implicit solution methods can be used to solve the governing equations, with different advantages and disadvantages [6]. For implicit forms, displacement is generally calculated as the primary variable and for explicit forms acceleration is calculated. Once the nodal solutions are calculated, the displacements and accelerations at the material points are calculated (mapped), the material points are moved and the background mesh is reset into its original position. To prepare for the next calculation step, the nodal values are mapped from the material points.

In general, shape functions are used to map various quantities, and in most cases the conservation of momentum is used for kinematic mapping, such that

$$\mathbf{a}_p^t = \sum_{i=1}^{N_n} \frac{\mathbf{F}_i^t}{m_i} N_i(\mathbf{x}_p^t) \tag{5}$$

where p is a material point counter, i is a node counter, N_n is the number of nodes, m_i is the mass associated with a node i, $\mathbf{F}$ is the total nodal force, N_i is the nodal shape function and $\mathbf{x}$ is the position of the material point.

Again using the conservation of momentum, velocity is mapped back from the material points to the reset nodes by

$$\mathbf{v}_i^t = \frac{\sum_{p=1}^{N_p} N_i(\mathbf{x}_p^t) m_p \mathbf{v}_p^t}{m_i^t} \tag{6}$$

where N_p is the number of material points and m_p is the mass of a material point.

2.3 Material model

A simple material model has been utilised here to explore the impact of simple post-peak material behaviour. The model is linear elastic prior to peak and cohesion strain-softening post-peak. The von Mises yield/failure surface has been adopted.

The plastic part of the material model is presented in Fig. 1. The material yields when the von Mises equivalent stress ($\sqrt{3J_2}$, where J_2 is the second shear stress invariant), equals the peak cohesion, c_p. After initial yield, the material softens at the rate of H per unit of the plastic shear strain invariant $\bar{\varepsilon}_p$, until reaching the residual cohesion, c_r, whereupon $\bar{\varepsilon}_p = \bar{\varepsilon}_{pr}$
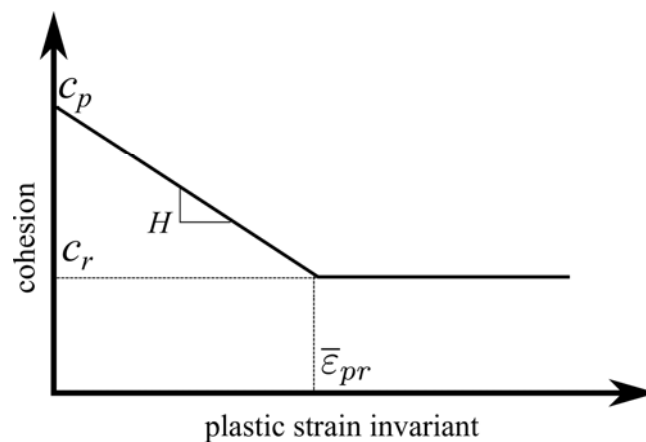

Fig. 1. Schematic of the strain-softening constitutive model [2].

3. Numerical modelling investigation

A typical cutting was investigated in this section as outlined in Fig. 2. The 45° cutting was 5 m deep, and founded on a strong bedrock. The bedrock was represented via a frictional boundary condition at the base, with a friction coefficient of 0.3. The lateral extent of the initial slope was 15 m and, at the lateral boundary, roller boundary conditions were imposed. The background grid, indicated in Fig. 2. by the grey squares, was 20 elements vertically and 80 horizontally. There were 4040 material points, with initially 4 material points per full element. The timestep was fixed at 5 x 10^{-3} s and the analysis was run until quasi-static conditions prevailed.

A total stress analysis was undertaken in this investigation and the material properties are given in Table 1. The first four properties were fixed in each analysis, whereas the residual cohesion and softening modulus were varied. The factor of safety of the slope is 0.96, based on peak cohesion, so that it fails under its self-weight.
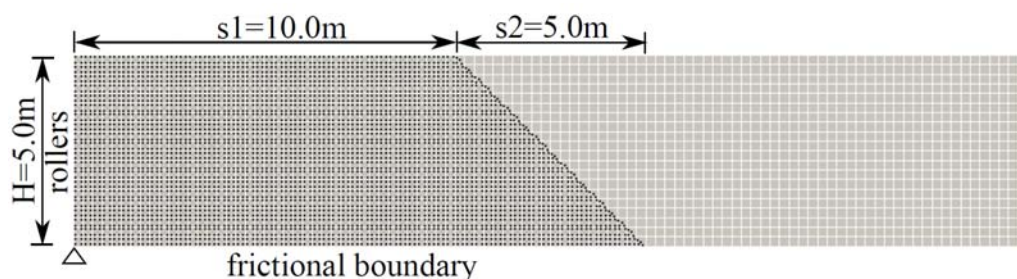

Fig. 2. Initial geometry, discretisation and boundary conditions [6].

Table 1 Material properties used in the simulations

Parameters	Values
Young's modulus	1 000 kPa
Poisson's ratio	0.33
Volumetric weight	20.0 kN/m^3
Peak cohesion	20.0 kPa
Residual cohesion	4, 8, 12 kPa
Softening modulus	25, 50, 75 kPa

Fig. 3 presents the final positions of the slopes for a variety of residual cohesions (12, 8 and 4 kPa), with the softening modulus fixed at 50 kPa. It is seen in Fig. 3(a) that, while a complete shear band is shown, only very limited slumping is exhibited at the slope crest. In this case, while slope maintenance may be required, only limited damage would most likely occur. In Fig. 3(b) a single complete slip circle is exhibited, along with additional minor failures at the back scarp. Looking down on the slope surface this would give the appearance of a single slip surface with slumping a short distance back from the rear scarp. The final analysis, with the lowest residual cohesion, gives a failure which retrogresses until the boundary condition gives support. Graben and horst features typical of spreads [7,8] are observed. In this case, any structure on top of the cutting or in front of the slope would most likely be damaged.
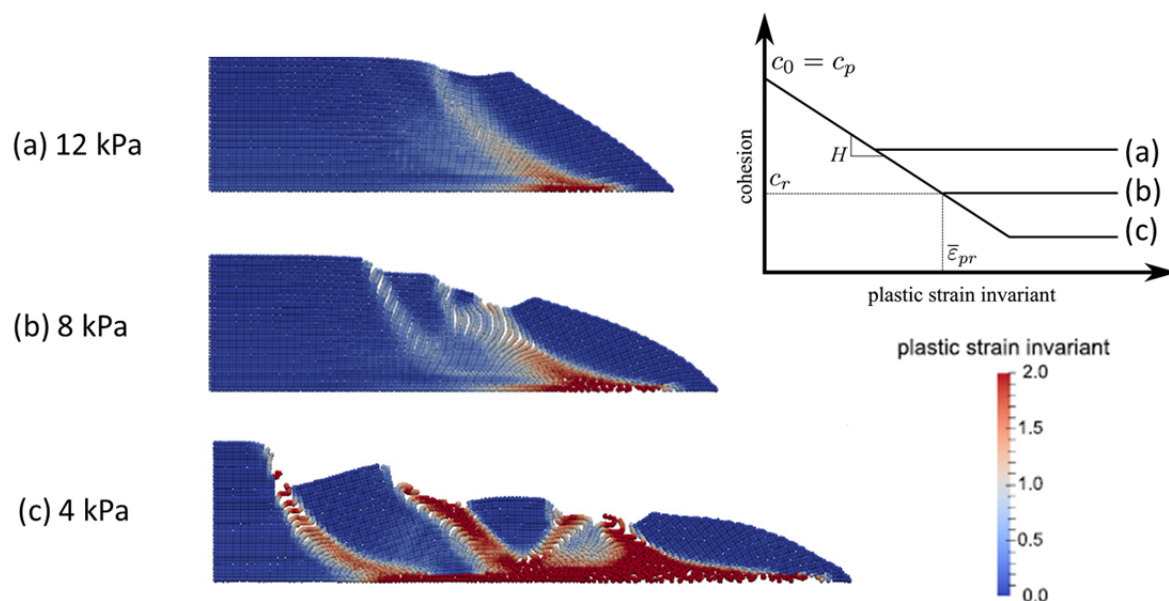

Fig. 3. Final positions of slope failure simulations, with differing residual cohesions.

The influence of the softening modulus on the final slope position is presented in Fig. 4, in which the lowest residual cohesion (4 kPa) is used in all of the simulations. Very clear shear bands and slip circles are shown in all of the simulations. As the softening modulus increases (Fig. 4(a) to 4(c)) the amount of retrogression increases. In all cases, spread type features are observed, albeit significantly limited in Fig. 4(a). In Fig. 4(c) the majority of the material exhibits a significant amount of plastic shear straining, with only a limited amount of material exhibiting elastic behaviour. In this case, the slope failure reaches the end of the domain.
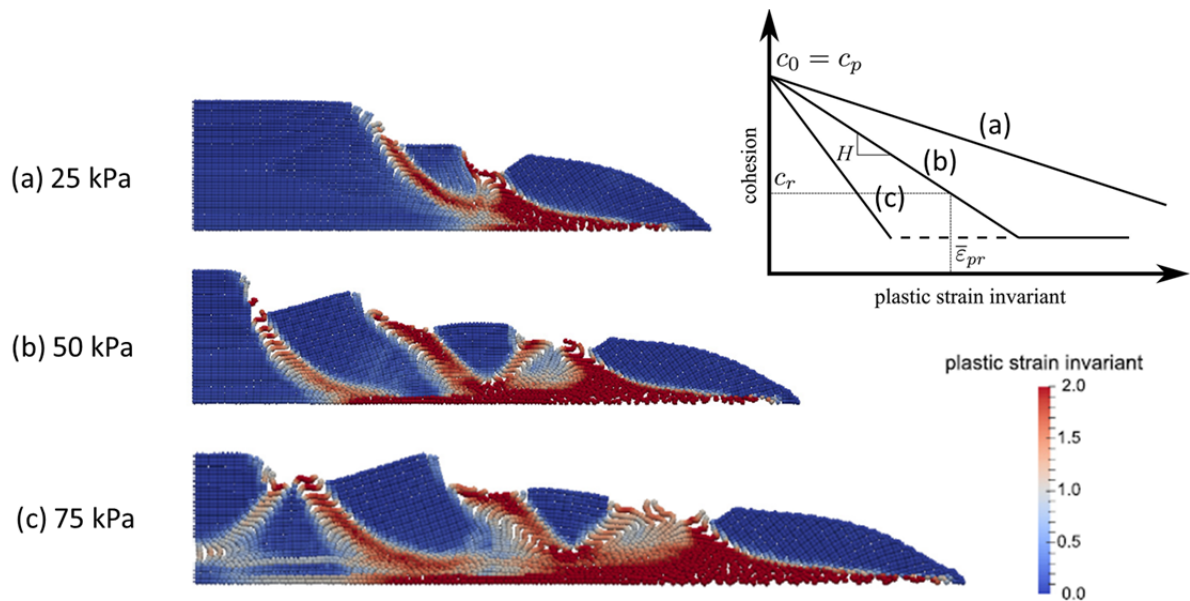
Fig. 4. Final positions of slope failure simulations, with differing softening moduli.

To explore how the constitutive model is behaving spatially, the controlling parts of the model have been spatially plotted for a single simulation (c_r = 4 kPa, H = 50 kPa) in Fig. 5. From Fig. 5(a) the first shear band can be seen progressing from the toe to the surface, with only a small part of the band having more than the residual strength remaining. The second shear band is also seen to be forming (softening), although almost no surface deformation is yet associated with it. In Fig. 5(b) the second shear band has completely formed, but the failure volume associated with the first slip is still in motion and only limited unloading has occurred. In Fig. 5(c) the first two failure volumes have finished their relative motion (they are still sliding along the bottom boundary) and unloading in the vicinity of the shear failures has occurred. A final shear band is formed near the vertical boundary.

While the performance of slope failure simulations has been seen to be governed by post-peak or post-failure behaviour, there is only very limited experimental or conceptual characterisation of such behaviour.
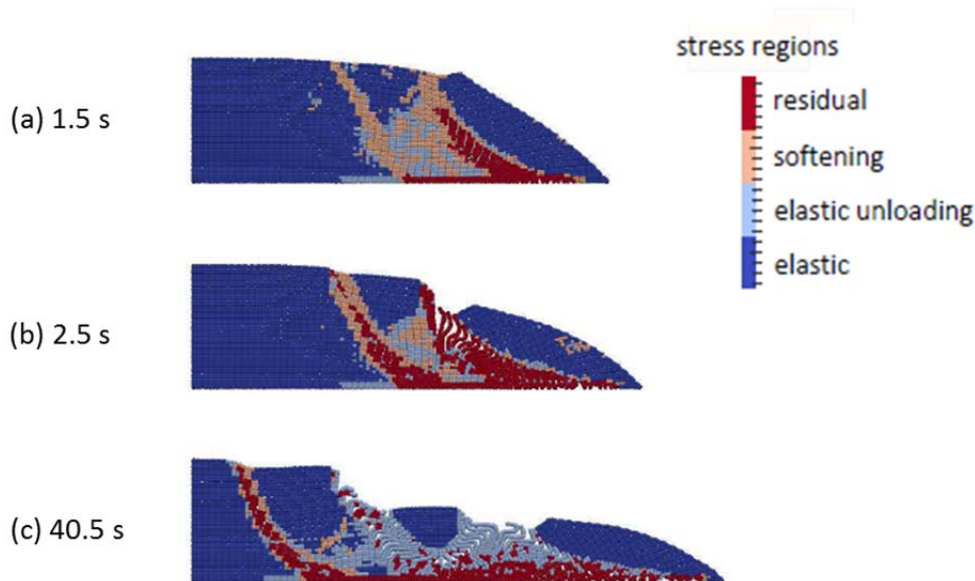

Fig. 5. Constitutive model stress regions at various times for a single simulation.

4. Conclusions

The ability of the material point method to simulate the entire failure process of slopes has been demonstrated. The importance of considering the post-failure behaviour in failure simulations has also been highlighted, with the risk associated with failure being strongly linked to post-peak shear strengths. To fully exploit such contemporary numerical modelling techniques, further developments in estimating or characterising post-failure material behaviour are needed.

Acknowledgements

References

[1] Sulsky, D., Chen, Z., Schreyer, H.L. A particle method for history-dependent materials, Comput. Meth. Appl. Mech. Engng., 1994, 118, 179–196.
[2] Wang, B., Vardon, P.J., Hicks, M.A., Chen, Z. Development of an implicit material point method for geotechnical applications, Comput. Geotech., 2016, 71, 159–167.
[3] Wang, B., Vardon, P.J., Hicks, M.A. Investigation of retrogressive and progressive slope failure mechanisms using the material point method, Comput. Geotech., 2016, 78, 88–98.
[4] Wang, B., Hicks, M.A., Vardon, P.J. Slope failure analysis using the random material point method, Géotechnique Letters, 2016, 6(2), 113–118.
[5] Wang, B., Vardon, P.J., Hicks, M.A. Preliminary analysis of rainfall-induced slope failures using the material point method, In Landslides and Engineered Slopes, Experience, Theory and Practice, Proceedings of the 12th International Symposium on Landslides, Naples, Italy, 2016, 2037–2042.
[6] Wang, B. Slope failure analysis using the material point method, PhD Thesis, Delft University of Technology, 2017.
[7] Van Asch, T., Brinkhorst, W., Buist, H., Vessem, P. The development of landslides by retrogressive failure in varved clays, Zeitschrift fur Geomorphologie, 1984, NF, 4, 165–181.
[8] Locat, A., Leroueil, S., Bernander, S., Demers, D., Jostad, H.P., Ouehb, L. Progressive failures in eastern Canadian and Scandinavian sensitive clays, Can. Geotech. J., 2011, 48, 1696–1712.